

Non-Invasive Cerebral Hemorrhage Size Determination by Microwave Signal Based on RSSD

Dequan Ding¹, Qinwei Li^{1*}, Jingyao Liu¹, Ming Yu², Hang Wu²

¹Tianjin Key Laboratory for Advanced Signal Processing, School of Electronic Information and Automation, Civil Aviation University of China, Tianjin, China

²Systems Engineering Institute, Academy of Military Science, People's Liberation Army, Tianjin, China

Email: *qw_li@cauc.edu.cn, ddq0124@163.com, ljyz_1632022@163.com, yuming_1990@outlook.com, 2008.wuhang@163.com

How to cite this paper: Ding, D.Q., Li, Q.W., Liu, J.Y., Yu, M. and Wu, H. (2024) Non-Invasive Cerebral Hemorrhage Size Determination by Microwave Signal Based on RSSD. *Journal of Computer and Communications*, 12, 224-240.

<https://doi.org/10.4236/jcc.2024.1211016>

Received: November 8, 2024

Accepted: November 26, 2024

Published: November 29, 2024

Abstract

Aiming at the prediction of the size of human cerebral hemorrhage point, a signal processing method based on Resonance Sparse Decomposition (RSSD) algorithm is proposed to decompose and analyze the microwave echo signal. According to the organizational structure of the human brain, a complete human brain model was established, and bleeding points of different sizes were placed at the same position, and 5 antennas were placed around the model (front, back, left, right, and top). RSSD is performed on the obtained echo signal, and Hilbert envelope analysis is performed on the low resonance component obtained by the decomposition, and then the size of the bleeding point is judged. Using CST and MATLAB to conduct simulation analysis and experiments, it is verified that the proposed method can successfully determine the size of the bleeding point, and the effectiveness and feasibility of the method are proved.

Keywords

Human Brain, Bleeding Point, Microwave, Resonance Sparse Decomposition

1. Introduction

Cerebral hemorrhage, also known as stroke, is the third leading cause of morbidity and mortality in many countries. Stroke is mainly divided into two categories, one is ischemic and the other is hemorrhagic. An ischemic stroke is due to loss of blood supply to an area of the brain. This is a common type of stroke. A hemorrhagic stroke is bleeding in the brain due to rupture of a blood vessel [1]. Routine

cerebral hemorrhage detection is mainly Computed Tomography (CT) or Magnetic Resonance Imaging (MRI) [2] [3].

The size of the bleeding spot in cerebral hemorrhage can vary with individual differences and specific circumstances. In general, the size of the bleeding point of cerebral hemorrhage can vary from tiny to large. Tiny bleeding spots may only affect a small part of the brain and may not cause noticeable symptoms. Larger hemorrhages may involve more extensive brain regions, potentially leading to severe neurological deficits.

The size of the bleeding point is usually determined by neuroimaging studies, such as head CT scan or MRI [2]-[5]. A deep learning framework based on U-net is proposed to automatically detect and segment hemorrhagic stroke in CT brain images [2]. Convolutional neural network was used to classify cerebral hemorrhage from head CT scan, and the model achieved the highest accuracy of 99.10%, improving the accuracy and speed of diagnosis [3]. An automatic detection method based on morphology and threshold segmentation is proposed to calculate the location and size of hemorrhagic spots according to the image features of different sequences in magnetic resonance images [4]. Doctors will evaluate the size and location of the bleeding point and the degree of impact on brain function based on the imaging results, and formulate a corresponding treatment plan. CT and MRI detection equipment are widely used clinically because of their unique diagnostic value, but they have their own defects. CT scans use X-rays. Although the dose is low, patients are still exposed to ionizing radiation. Especially with repeated or multiple scans, the accumulation of radiation can pose a potential risk to the patient's health. MRI scans typically take a long time and are restrictive in certain patients, such as people with pacemakers, internal metal objects, or other implants, making them inappropriate and expensive.

Intracerebral hemorrhage point target detection, in essence, is a kind of fault diagnosis. Resonance sparse decomposition algorithm is a relatively new signal processing method, which is different from the traditional signal processing method based on frequency or size. In the process of realizing the feature extraction of vibration signal, the method considers both the frequency and bandwidth of the signal. The components of vibration signal are understood as periodic harmonics, fault shock and noise, and separated into high and low resonance components and residual components respectively. At present, the resonance sparse decomposition algorithm is mainly used in the fault diagnosis of bearings, and carries out resonance sparse decomposition of bearing signals to obtain high resonance component and low resonance component. The Hilbert envelope spectrum demodulation analysis is carried out on the low resonance component to extract the fault characteristic frequency, and then the fault diagnosis of the rolling bearing is carried out [6]-[10].

Compared with mainstream detection methods, microwave technology can be used for non-destructive detection of stroke, and the price is low. Hemorrhagic stroke will change the dielectric properties of the tissue [11], which will change

the reflection and absorption of microwaves. According to this electromagnetic property, it is possible to detect stroke with microwaves. In existing techniques, microwave detection begins by placing an array of microwave antennas around the brain. The signals transmitted and received by the antenna are processed accordingly. To analyze the size and location of the bleeding spot in the brain [11]-[20].

2. Materials and Methods

2.1. Resonance Sparse Decomposition

Resonance Sparse Decomposition (RSSD) is a newly proposed signal decomposition algorithm, which is different from the traditional signal decomposition algorithm (wavelet decomposition). RSSD takes both the frequency and bandwidth of the signal into account when decomposing the signal. Tunable Q factor wavelet transform (TQWT) is used to represent the high and low quality factors of the signal according to the different quality factors of the harmonic signal and the fault impact signal. The signals are then separated nonlinearly by morphological component analysis (MCA) [6]. The quality factor Q can be defined as

$$Q = \frac{f_c}{B} \quad (1)$$

In (1), f_c is the center frequency of an oscillation of the signal, and B is its bandwidth.

According to the signal quality factor Q , it is decomposed into high resonance component, low resonance component and residual component. The high resonance component has a large Q value and good frequency aggregation, which represents the harmonic component; the low resonance component has a small Q value and poor frequency aggregation. Represents the transient shock classification (fault component).

Assuming that the signal x is formed by a linear combination of K different morphological feature components, each component corresponds to a complete dictionary, so the initial signal x can be expressed as

$$x = \sum_{k=1}^K x_k = \sum_{k=1}^K S_k W_k \quad (2)$$

In (2), S_k is an over-complete dictionary, and W_k is the coefficient of an over-complete dictionary.

First, TQWT is performed on the signal to obtain two sets of basis function libraries, and the corresponding transformation coefficients are obtained through iterative calculation. Then use MCA to establish the objective function of sparse decomposition, which can be expressed as

$$J(w_1, w_2) = \|x - S_1 w_1 - S_2 w_2\|_2^2 + \lambda_1 \|w_1\|_1 + \lambda_2 \|w_2\|_1 \quad (3)$$

In (3), and are the transformation coefficients of high-resonance classification and low-resonance components in S_1 and S_2 ; λ_1 and λ_2 are regularization parameters, and their magnitudes are related to the energy distribution of high-

and low-resonance components during decomposition. When the size of λ_1 is fixed, if the value of λ_2 is reduced, the energy distribution of the resonance component corresponding to λ_2 will increase. When the values of λ_1 and λ_2 are reduced at the same time, the energy of the residual signal component will decrease.

Then, use the SALS algorithm to perform iterative operations on the above equations, and update the transformation coefficients to obtain the minimum objective function. When the dissipation function is minimized, the optimal coefficient matrices w_1^* and w_2^* are obtained. Finally, the sparse expressions $S_1 w_1^*$ and $S_2 w_2^*$ of the high and low resonance components in the original signal are reconstructed. The flowchart of RSSD is shown in **Figure 1**.

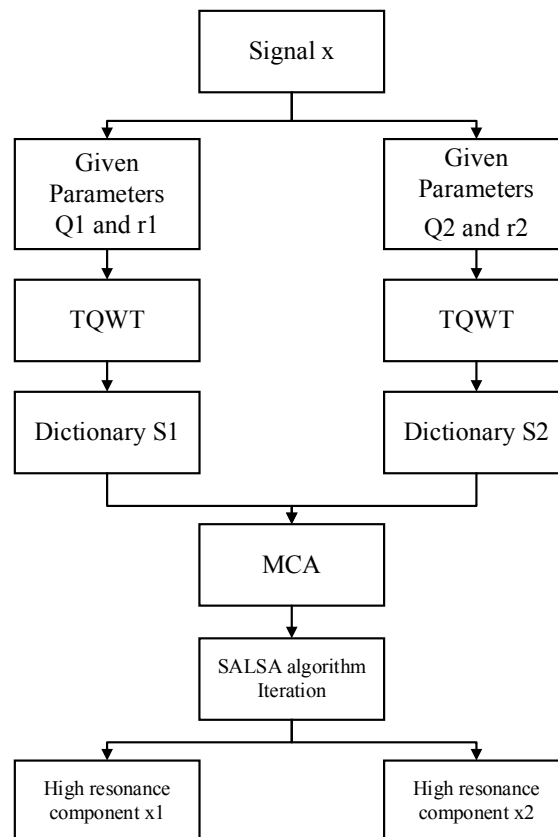


Figure 1. Resonance sparse decomposition algorithm flow chart.

2.2. Human Brain Modeling

The human brain is the center of the human nervous system. It has complex structure and functions and is one of the most important organs of the human body. It is responsible for controlling and regulating almost all physical and mental activities of the human body, including perception, thinking, memory, movement, emotion, etc. In order to study the physical phenomena inside the human brain more accurately, such as the reflection and absorption of microwaves by bleeding spots, a complete electromagnetic model of the human brain is established. The

established model is shown in **Figure 2**.

The anatomical structure of the human brain is very complex. According to the anatomy diagram of the human brain, it can be concluded that the human brain is composed of multiple parts. During simulations and experiments, the dielectric constant is one of the indicators that measures the ability of a medium to respond to an electric field. Therefore, selecting brain tissues with similar or equal dielectric constants for similar sensing can ensure that simulations and experiments are easy to conduct and can provide accurate and reliable results.



Figure 2. Complete human brain model.

In the human brain model, the brain is divided into different tissues, including cerebrospinal fluid, gray matter, white matter, skull, and skin. These tissues differ in structure and properties and respond differently to electromagnetic fields. The corresponding models of different tissues in the human brain are shown in **Figure 3**. Through the model in the illustration, we can better understand the structure of the human brain and the role of different tissues in simulations and experiments. Such a model can be used to study the propagation, scattering and absorption of electromagnetic fields in different tissues, providing an important reference for studying the electromagnetic properties of the human brain, disease diagnosis and treatment, etc. The corresponding dielectric constants and conductivities of different brain tissues are summarized into **Table 1**.

It can be seen from **Table 1** that the dielectric constant and conductivity of blood are significantly higher than the electromagnetic parameters of most brain tissues. Since blood exists in blood vessels under normal circumstances, once a rupture occurs, it will cause changes in electromagnetic parameters in the nearby area, thereby affecting the propagation of microwave signals. In general, the composition of the human brain is very complex. Simulation and experimentation of brain tissue based on similar or equal dielectric constants can ensure easy operation, accuracy and reliability.

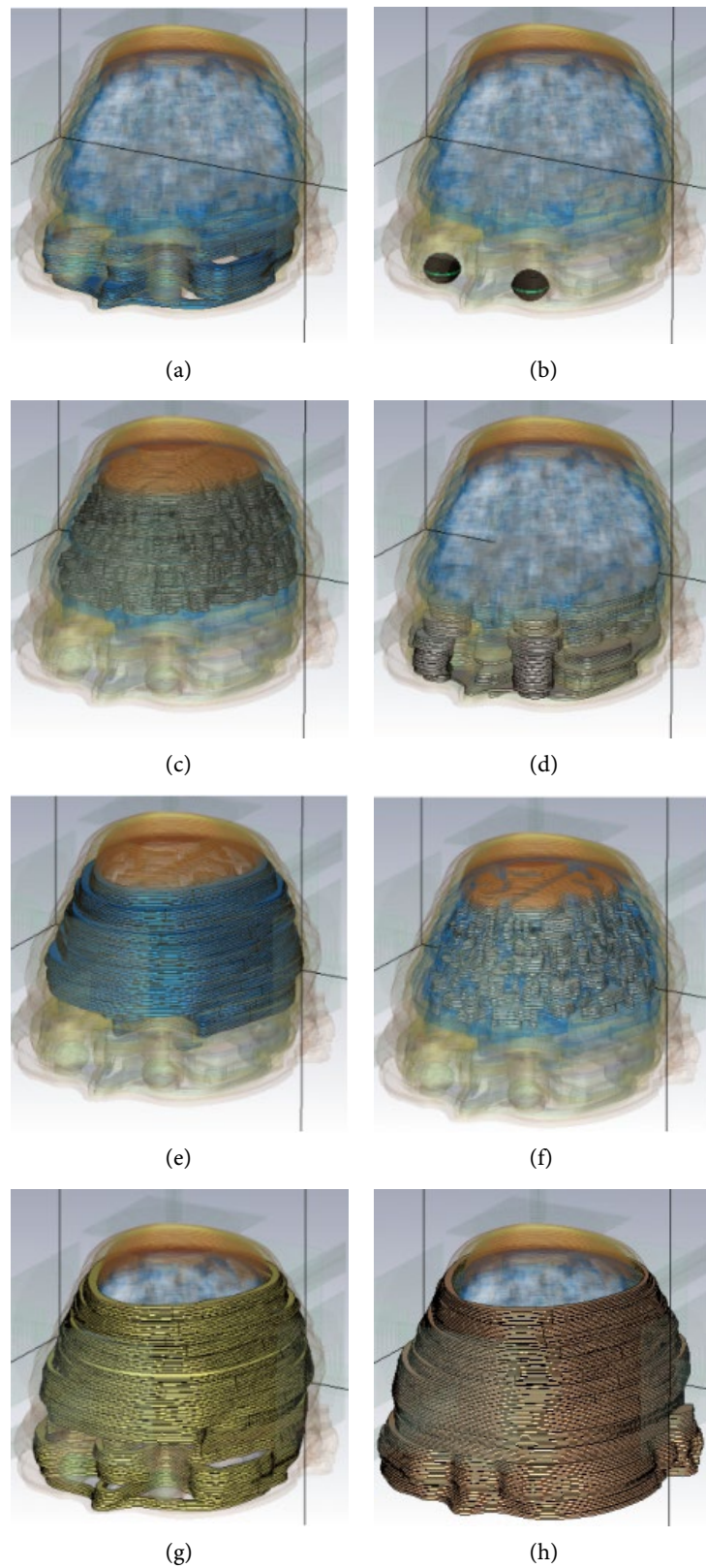


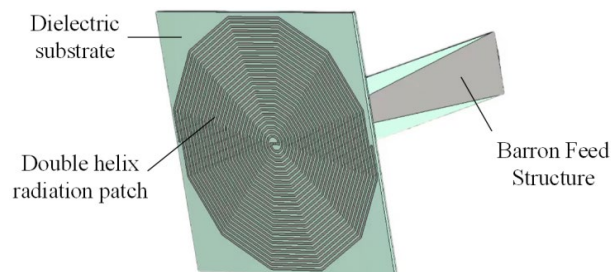
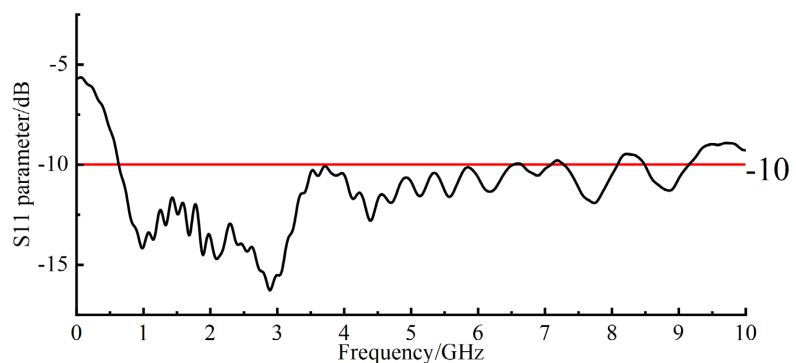
Figure 3. The components of the human brain: (a) lower cerebrospinal fluid, (b) eyeball, (c) gray matter, (d) brain parenchyma, (e) upper cerebrospinal fluid, (f) white matter, (g) skull, (h) skin.

Table 1. Corresponding permittivity of different brain tissues.

Brain tissue	Dielectric constant ϵ_r	Conductivity σ (S/m)
Cerebrospinal fluid	68	2.5
Eyeball	5.447	0.053
Gray matter	52.282	0.985
Brain parenchyma	42	0.7
White matter	46	0.82
Skull	12	0.2
Skin	40.936	0.089
Blood	61	1.6

2.3. Antenna Design

The antenna used in this experiment is “dodecagon Archimedean spiral antenna”. It is a small size ultra-wideband antenna. The antenna operates at a frequency of 0.6 - 6.5 GHz. The gain in the working range is 2 - 5 dBi, which basically meets the experimental requirements. The main radiant area of the antenna consists of a 60 mm \times 60 mm dielectric substrate and a dodecagon Archimedean spiral radiator. The feed mode of the antenna adopts Barron feed structure, which realizes the impedance matching between coaxial line and radiator and the conversion of unbalanced signal to balanced signal. **Figure 4** shows the structure of the antenna used. **Figure 5** shows the simulation results of the return loss (S11) of the antenna.

**Figure 4.** Antenna model.**Figure 5.** The return loss of the antenna (S11).

3. Experimental Simulation

A bleeding spot with a radius of 5 mm was placed on the upper left of the complete electromagnetic model of human brain. The location of the bleeding point is shown in **Figure 6**. Then change the size of the bleeding point at the same position, and the changed sizes are 8 mm, 11 mm, and 14 mm respectively. Simulation experiments are carried out on the above five models (including the model without bleeding point).

The model was simulated after the hemorrhagic sites were placed. The input signal is a single Gaussian pulse signal, and five sets of output signals (o1, 1) are obtained after simulation, as shown in **Figure 7**.

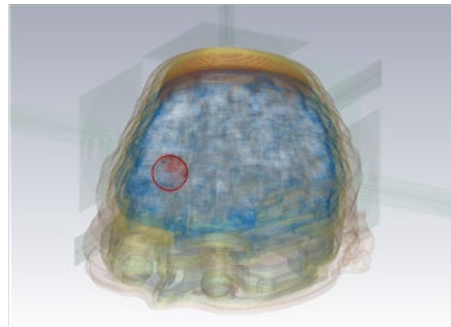
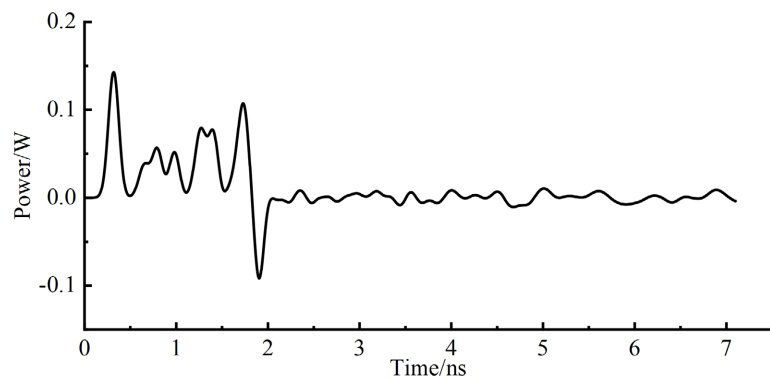
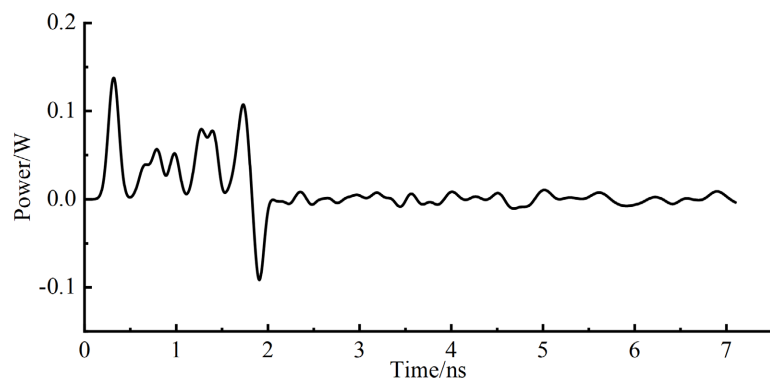


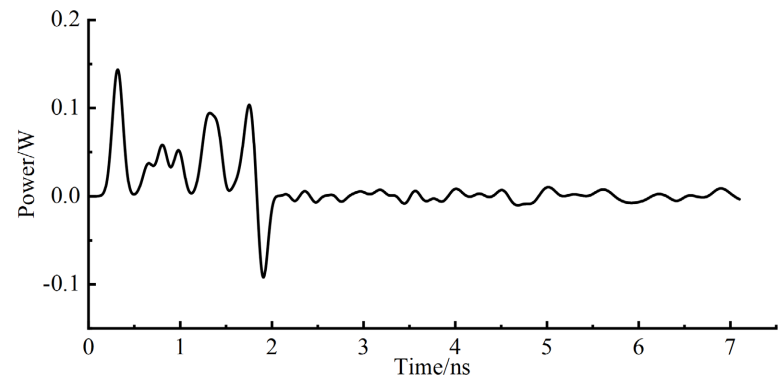
Figure 6. 5 mm bleeding point human brain model.



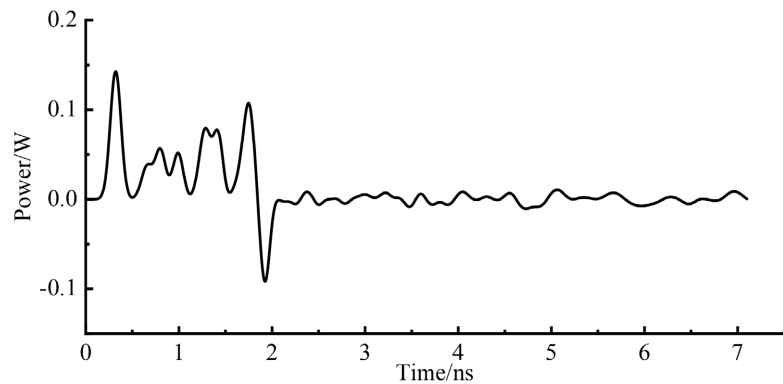
(a)



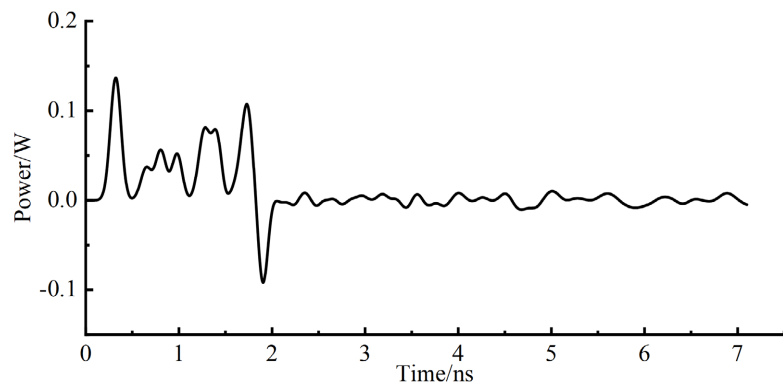
(b)



(c)



(d)



(e)

Figure 7. Five groups of output signal (o1,1) waveforms: (a) no bleeding point o1,1; (b) 5 mm bleeding point o1,1; (c) 8 mm bleeding point o1,1; (d) 11 mm bleeding point o1,1; (e) 14 mm bleeding point o1,1.

From the five groups of o1,1 waveform diagrams obtained above, it is not difficult to see that there is little difference between the signals obtained from bleeding points of different sizes. This is because the bleeding point model is not an order of magnitude in size or complexity compared with the whole human brain model, so the difference reflected in the signal is very small. This also reflects the importance of extracting features by processing the signal.

The obtained simulation result data is exported. Considering that the original

excitation signal can only be a monopulse signal, the resulting o1,1 waveform is also the result of a monopulse signal. In order to simulate the actual signal waveform, input a multi-pulse signal. The o1,1 waveform graph is now periodically extended by 602 units points. Then the first 4096 points are taken for RSSD processing. The final waveform is shown in **Figure 8**.

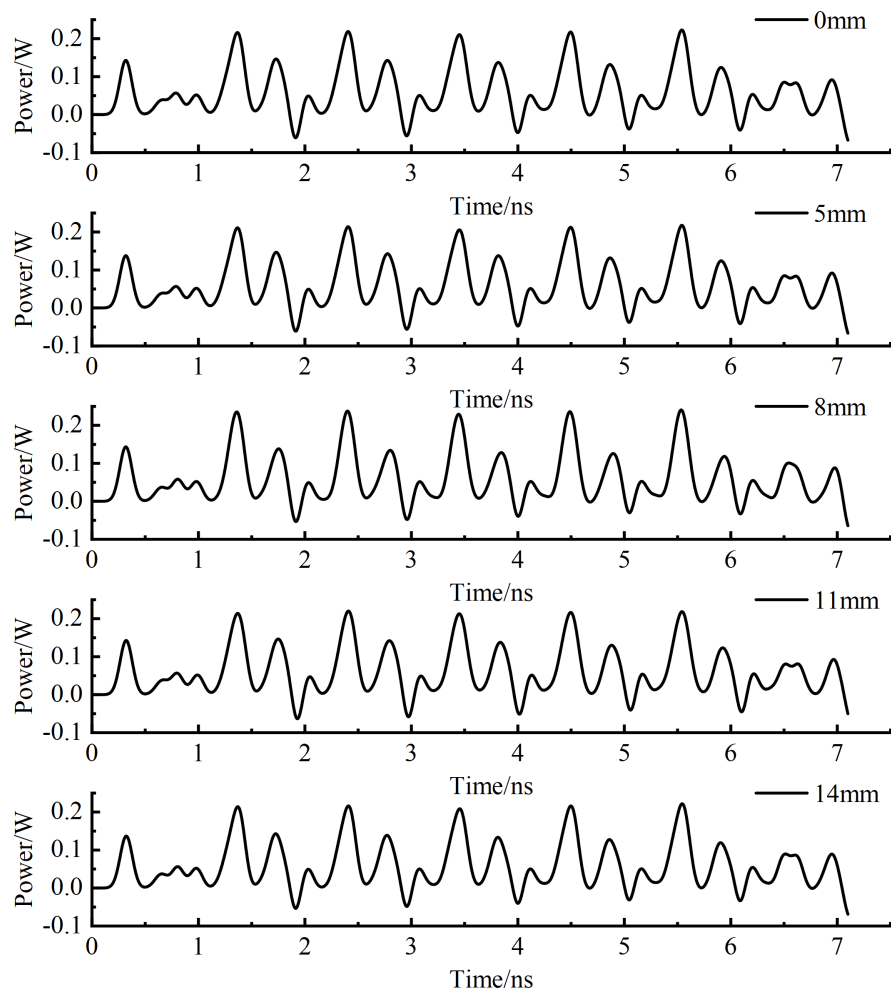
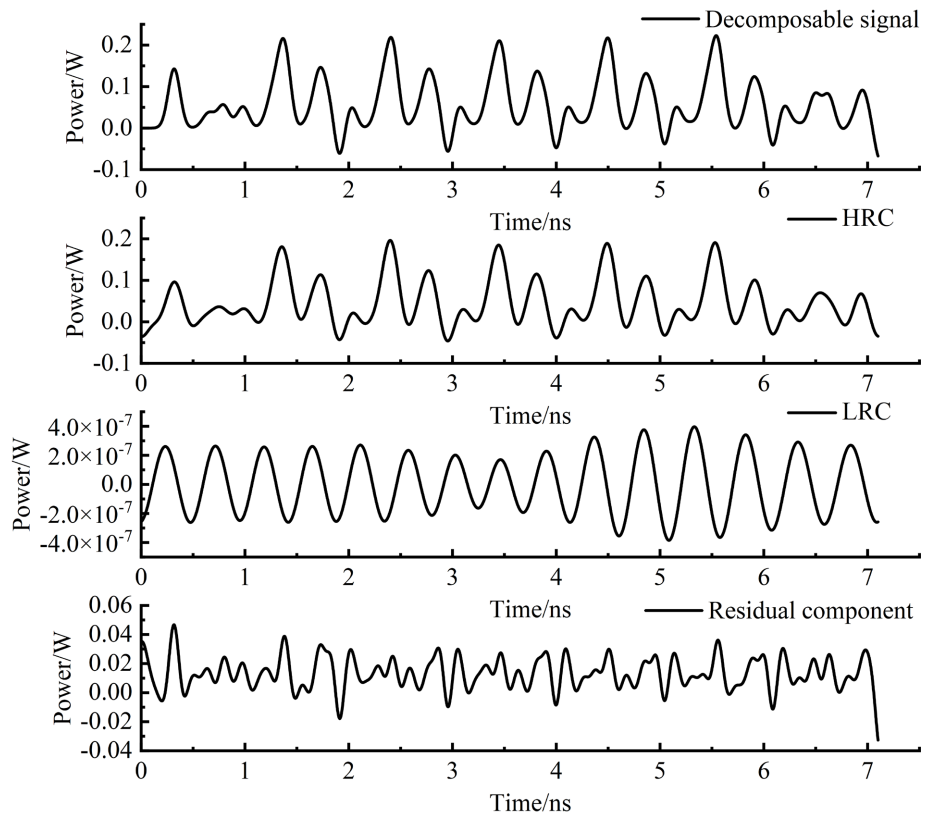


Figure 8. Waveform diagram of period extension of signal at different bleeding points.

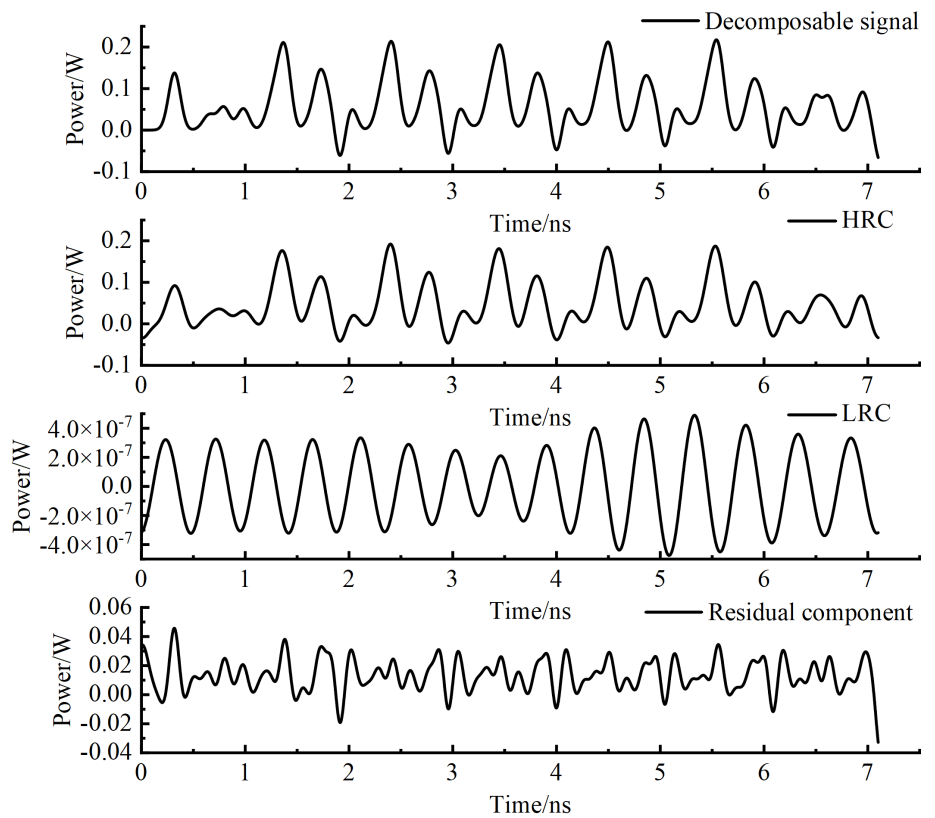
The resonance sparse decomposition algorithm mainly includes three parameters: quality factor Q , wavelet redundancy r , and decomposition layer number J . According to the decomposed signal waveform diagram and experience, quality factors $Q_1 = 6$, $Q_2 = 1$ and redundancy $r_1 = 12$, $r_2 = 25$ can be preliminarily selected. The maximum value of the number of decomposition layers J is determined as

$$J_{max} = \left\lfloor \frac{\log(\beta N / 8)}{\log(1/\alpha)} \right\rfloor \quad (1)$$

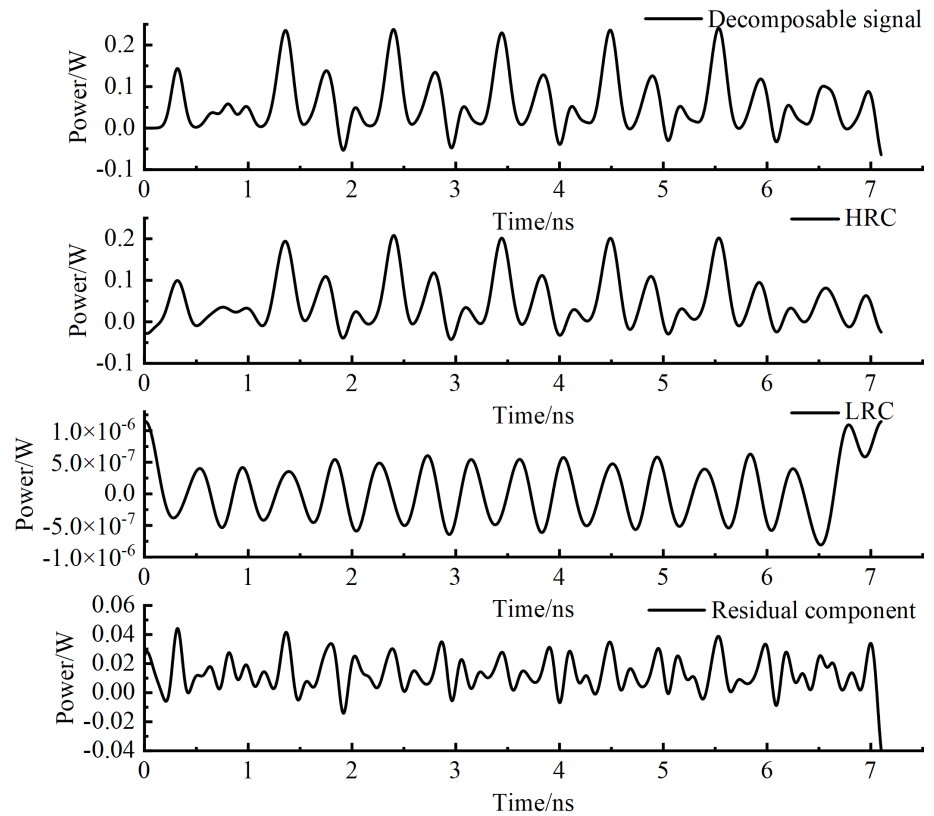
In (4), $\lfloor * \rfloor$ represents the largest integer that does not exceed the number in parentheses, and N is the signal length.



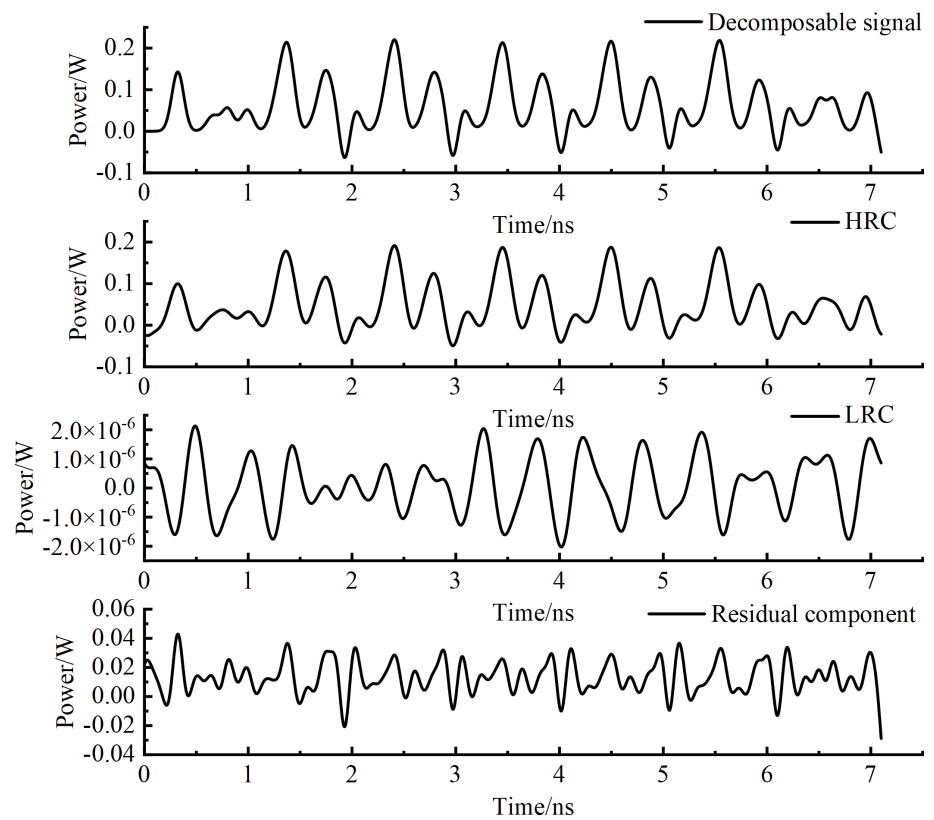
(a)



(b)



(c)



(d)

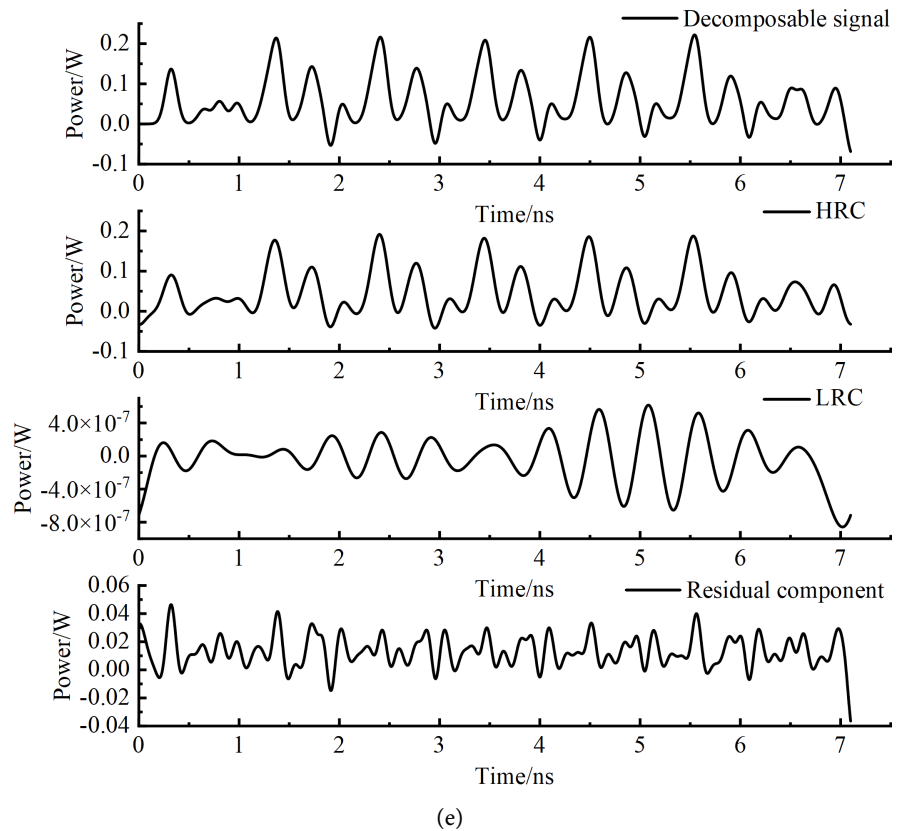


Figure 9. Signal resonance sparse decomposition results: (a) Signal decomposition results without bleeding points, (b) Signal decomposition results of 5 mm bleeding points, (c) Signal decomposition results of 8 mm bleeding points, (d) Signal decomposition results of 11 mm bleeding points, (e) 14 mm bleeding points Signal Decomposition Results.

After the parameters are determined, the signal to be decomposed is subjected to resonance sparse decomposition, and the decomposition results of the five signals to be decomposed are shown in **Figure 9**. The first of each graph is the band decomposition signal, the second is the high resonance component after the RSSD, the third is the low resonance component, and the last is the residual component.

It can be seen from the above figure that there is almost no difference between the high resonance components in the decomposition results of the five groups, and there are obvious differences in the low resonance components. Next, the five groups of low resonance components are further processed and analyzed.

First of all, in order to limit the preprocessed data to a certain range, so as to eliminate the adverse effects caused by singular sample data. The low resonance component is normalized, and the result is shown in **Figure 10**.

The obtained normalized data is subjected to envelope extraction (Hilbert transform), and then fast Fourier transform (FFT) is performed on it. The obtained results are shown in **Figure 11**. Due to the large number of points, only the FFT results of the first 50 points are presented in the figure for ease of observation.

To see the trend more clearly. The second highest amplitude point of each picture in **Figure 11** was extracted and **Figure 12** was drawn.

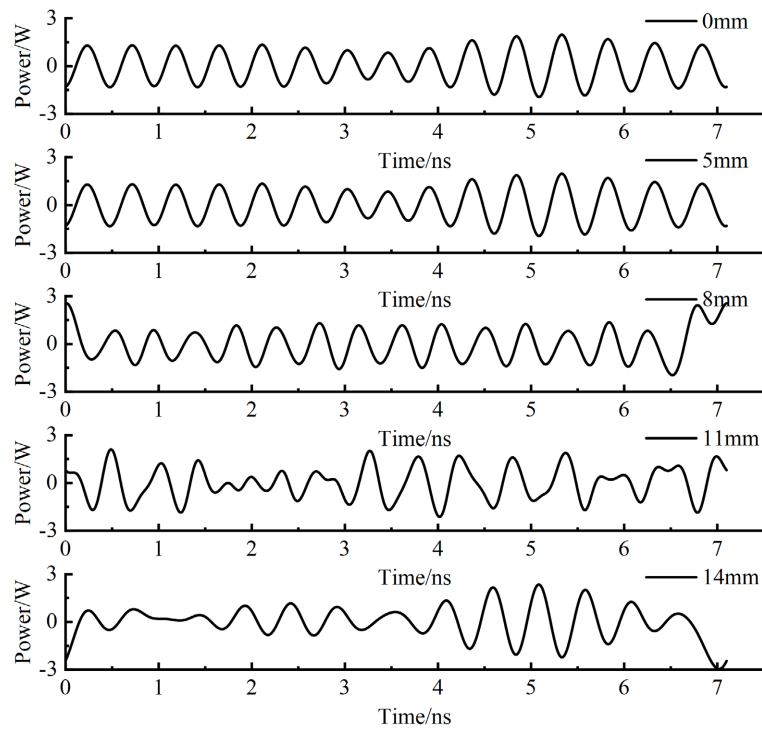


Figure 10. The results of normalization of low resonance components.

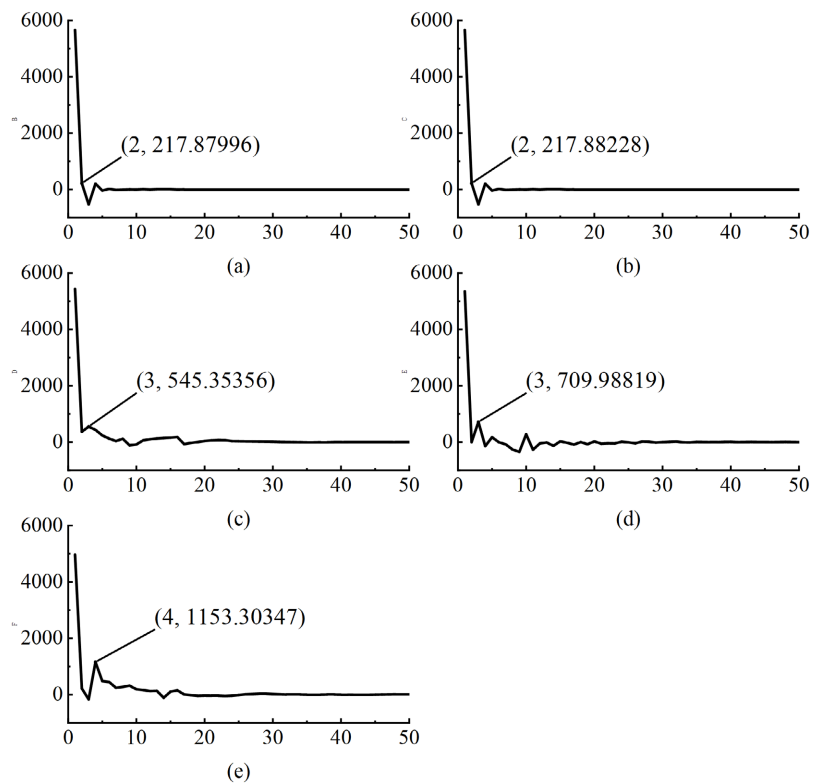


Figure 11. The real part of the envelope spectrum of the low resonance component of signals with different bleeding points: (a) Signal without bleeding points, (b) Signal of 5 mm bleeding points, (c) Signal of 8 mm bleeding points, (d) Signal 11 mm bleeding points, (e) Signal 14 mm bleeding points.

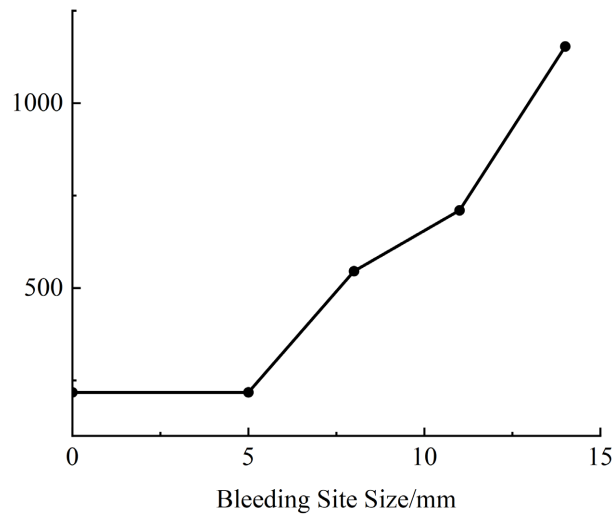


Figure 12. The second highest amplitude point is extracted.

It is not difficult to see from the result graph that with the increase of the bleeding point, the value of the second highest amplitude point of the real part of the envelope spectrum of the low resonance component of different bleeding point signals is getting larger and larger, and there is a tendency to gradually delay.

4. Conclusion

This experiment is based on the signal analysis of cerebral hemorrhage points of different sizes based on the resonance sparse decomposition algorithm. Firstly, the cycle extension is carried out on the modeling and simulation results obtained, and then the signal is decomposed on the basis of selecting important parameters. The decomposed signals of low resonance components with obvious differences are processed by normalization, envelope extraction and FFT. Finally, with the increase of the bleeding point, the value of the second highest amplitude point of the frequency domain signal is getting larger and gradually moving backward. An important conclusion can be drawn that the larger the bleeding point, the higher the value of the second highest amplitude point in the frequency domain.

Conflicts of Interest

The authors declare no conflicts of interest regarding the publication of this paper.

References

- [1] Unnithan, A.K.A., Das, J.M. and Mehta, P. (2022) Hemorrhagic Stroke. Stat Pearls Publishing LLC.
- [2] Li, L., *et al.* (2021) Deep Learning for Hemorrhagic Lesion Detection and Segmentation on Brain CT Images. *IEEE Journal of Biomedical and Health Informatics*, **25**, 1646-1659. <https://doi.org/10.1109/IBHI.2020.3028243>
- [3] Mahjoubi, M.A., Hamida, S., Siani, L.E., Cherradi, B., Abbassi, A.E. and Raihani, A. (2023) Deep Learning for Cerebral Hemorrhage Detection and Classification in Head CT Scans Using CNN. 2023 *3rd International Conference on Innovative Research in*

- Applied Science, Engineering and Technology (IRASET)*, Mohammedia, 18-19 May 2023, 1-8. <https://doi.org/10.1109/IRASET57153.2023.10153010>
- [4] Ruan, X., Shi, T., Chen, H. and Yao, H. (2020) Feature Extraction and Research Based on MRI Image of Cerebral Hemorrhage. 2020 *International Conference on Computer Network, Electronic and Automation (ICCNEA)*, Xi'an, 25-27 September 2020, 369-372. <https://doi.org/10.1109/ICCNEA50255.2020.00082>
- [5] Yi, X., et al. (2020) Application of CT Imaging in the Diagnosis of Cerebral Hemorrhage and Cerebral Infarction Nerve Damage. *World Neurosurgery*, **138**, 714-722. <https://doi.org/10.1016/j.wneu.2020.02.007>
- [6] Chen, J., Wang, L., Huang, Y., Li, Y. and Dong, D. (2022) Fault Diagnosis of Rolling Bearing Based on Optimal Resonance Sparse Decomposition. 2022 *Global Reliability and Prognostics and Health Management (PHM-Yantai)*, Yantai, 13-16 October 2022, 1-7. <https://doi.org/10.1109/PHM-Yantai55411.2022.9942209>
- [7] Chai, N., Yang, M., Ni, Q. and Xu, D. (2018) Gear Fault Diagnosis Based on Dual Parameter Optimized Resonance-Based Sparse Signal Decomposition of Motor Current. *IEEE Transactions on Industry Applications*, **54**, 3782-3792. <https://doi.org/10.1109/TIA.2018.2821099>
- [8] Huang, W., Sun, H., Liu, Y. and Wang, W. (2017) Feature Extraction for Rolling Element Bearing Faults Using Resonance Sparse Signal Decomposition. *Experimental Techniques*, **41**, 251-265. <https://doi.org/10.1007/s40799-017-0174-5>
- [9] Huang, W.T., Sun, H.J. and Wang, W.J. (2017) Resonance-Based Sparse Signal Decomposition and Its Application in Mechanical Fault Diagnosis: A Review. *Sensors*, **17**, 1279-1279. <https://doi.org/10.3390/s17061279>
- [10] Lu, Y., Du, J. and Tao, X. (2019) Fault Diagnosis of Rolling Bearing Based on Resonance-Based Sparse Signal Decomposition with Optimal Q-Factor. *Measurement and Control*, **52**, 1111-1121. <https://doi.org/10.1177/0020294019858181>
- [11] Behnaz, S., et al. (2020) Detection of Haemorrhagic Stroke in Simulation and Realistic 3-D Human Head Phantom Using Microwave Imaging. *Biomedical Signal Processing and Control*, **61**, 1746-8094. <https://doi.org/10.1016/j.bspc.2020.102001>
- [12] Haddad, W. and Trebes, J. (2002) Microwave Hemorrhagic Stroke Detector. US Patent No. 6454711.
- [13] Persson, M., et al. (2014) Microwave-Based Stroke Diagnosis Making Global Pre-hospital Thrombolytic Treatment Possible. *IEEE Transactions on Biomedical Engineering*, **61**, 2806-2817. <https://doi.org/10.1109/TBME.2014.2330554>
- [14] Crocco, L., Karanasiou, I., James, M. and Conceicao, R.C. (2018) Emerging Electromagnetic Technologies for Brain Diseases Diagnostics, Monitoring and Therapy. Springer International Publishing. <https://doi.org/10.1007/978-3-319-75007-1>
- [15] Merunka, I., Massa, A., Vrba, D., Fiser, O., Salucci, M. and Vrba, J. (2019) Microwave Tomography System for Methodical Testing of Human Brain Stroke Detection Approaches. *International Journal of Antennas and Propagation*, **2019**, 9. <https://doi.org/10.1155/2019/4074862>
- [16] Ireland, D. and Bialkowski, M. (2011) Microwave Imaging for Stroke Detection. *Progress in Electromagnetics Research M*, **21**, 163-175. <https://doi.org/10.2528/PIERM11082907>
- [17] Mohammed, B.J., Ireland, D. and Abbosh, A.M. (2012) Experimental Investigations into Detection of Breast Tumour Using Microwave System with Planar Array. *IET Microwaves Antennas & Propagation*, **6**, 1311-1317. <https://doi.org/10.1049/iet-map.2012.0178>

- [18] Candefjord, S., *et al.* (2017) Microwave Technology for Detecting Traumatic Intracranial Bleedings: Tests on Phantom of Subdural Hematoma and Numerical Simulations. *Medical & Biological Engineering & Computing*, **55**, 1177-1188. <https://doi.org/10.1007/s11517-016-1578-6>
- [19] Scapaticci, R., Donato, L.D., Catapano, I. and Crocco, L. (2012) A Feasibility Study on Microwave Imaging for Brain Stroke Monitoring. *Progress in Electromagnetics Research B*, **40**, 305-324. <https://doi.org/10.2528/PIERB12022006>
- [20] Scapaticci, R., Tobon, J., Bellizzi, G., Vipiana, F. and Crocco, L. (2018) Design and Numerical Characterization of a Low-Complexity Microwave Device for Brain Stroke Monitoring. *IEEE Transactions on Antennas and Propagation*, **66**, 7328-7338. <https://doi.org/10.1109/TAP.2018.2871266>